

Micromagnetic simulations of spin-wave normal modes and the resonant field-driven magnetization dynamics of a 360° domain wall in a soft magnetic stripe

P. E. Roy*

Hitachi Cambridge Laboratory, Cambridge CB3 0HE, United Kingdom

T. Trypiniotis and C. H. W. Barnes

Cavendish Laboratory, Cambridge University, Cambridge CB3 0HE, United Kingdom

(Received 9 February 2010; revised manuscript received 25 August 2010; published 7 October 2010)

Spin normal modes of a 360° domain wall trapped in a stripe are investigated by micromagnetic simulations, for two in-plane field excitation directions. Within the substructure of the 360° domain wall, we identify highly localized, low-frequency spin-wave well-type modes on the lateral boundaries and in the surrounding subdomain walls. At intermediate frequencies, oscillations distributed over a range of modes located in different regions of the substructure's domain walls are found. Higher-frequency oscillations such as quasiuniform and multinodal spin-wave modes are identified inside each of the constituent subdomains. Mode splitting due to interaction with traveling spin waves is found. Indications are that domain mode quantization due to confinement effects induced by the constituent domain walls are relatively weak. Strong hybridization between domain and domain-wall modes are likely to occur within a certain frequency interval. Finally, we resonantly drive the system at the four lowest frequency modes, whereby the in-plane behavior of the 360° structure displays translational, breathing, and wobbling motions.

DOI: [10.1103/PhysRevB.82.134411](https://doi.org/10.1103/PhysRevB.82.134411)

PACS number(s): 75.78.Cd, 75.78.Fg

I. INTRODUCTION

The 360° domain wall (DW), which is a composite object consisting of two coupled oppositely polarized transverse DWs (Ref. 1) is mostly mentioned in relation to an incomplete reversal in a magnetic element. It can, for instance, form when attempting to reverse the magnetization in a nanostripe from a remanent C state. Once formed, it resists the completion of the reversal over a rather large field interval, significantly increasing the switching field. It is therefore thought of as a nuisance from a device point of view. There are however potential applications of such a DW. Hertel *et al.* found that when spin waves (SWs) pass through a 360° DW, they can be phase shifted by 180° .² Therefore, it should, in principle, be possible to use these DWs as components in SW interference devices. To effectively use the DW as a phase shifter, information on its frequency response is important. An additional potential usage is as bit storage entities since the constituents of the 360° DW, may act as a logical "1" and "0." A device geometry whereby they could be placed is in stripes. Recently, Mascaro *et al.* conducted micromagnetic simulations on the interaction between a transverse DW (TDW) and a 360° DW in a multilayer stripe and found that the stray field from a 360° DW in the hard layer could effectively act as a pinning site for a TDW in the free layer.³ The advantage over geometrical constrictions as a pinning site is that it should be experimentally possible to create and annihilate a 360° DW at will. The creation can, for instance, be accomplished by engineered TDW collisions.⁴ Annihilation of the DW could efficiently be achieved by using a spin-polarized current, whereby the whole DW structure should move in a translational manner along the stripe to finally be pushed out at the far edge. Additional applications may be that of SW generation and multiplication; Hermsdoerfer *et al.* showed by micromag-

netic simulations that a pinned TDW could act as a spin-wave frequency doubler, whereby it emits SWs at twice the frequency of its own resonance frequency.⁵ Therefore, apart from a fundamental interest, there are reasons to study the frequency response of 360° DWs. There has not to date been a systematic study of the normal modes and field-driven oscillations of the 360° DW. Muratov and Osipov theoretically investigated their stability and reversal mechanisms in confined geometries.⁶ From a dynamics point of view, Shamsudinov and Nazarov theoretically probed some aspects of small oscillation vibrations of a 360° DW in a massive uniaxial ferromagnet with a large quality factor.⁷ However, the dynamical behavior in soft magnetic, geometrically confined structures remains to be uncovered. In this paper, we perform micromagnetic simulations to explore the normal modes of a 360° DW trapped in a permalloy stripe as a result of uniform field perturbations. Further, we drive the DW at resonance and visualize the corresponding DW motion. The simulations are performed with our own code whose characteristics are described in the next section. A previous version of the code was benchmarked against the micromagnetic standard problem 4.⁸ Comprehensive benchmarking of the current version can be found in the supplementary material where it shows very good agreement to the OOMMF package⁹ for a test problem covering both static and dynamic cases.¹⁰

II. MICROMAGNETIC TECHNIQUE AND SIMULATION DETAILS

Within the micromagnetic approach the magnetization of a sample is represented by a magnetization vector $\mathbf{M}(\mathbf{r})$ that varies continuously with position, with a magnitude equal to the material's saturation magnetization M_s . In this work we use Cartesian coordinates with $\mathbf{M}=(M_x, M_y, M_z)$, where the axes are oriented according to Fig. 1. The interaction energy

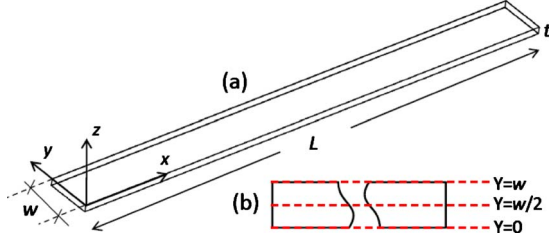


FIG. 1. (Color online) (a) Schematic depicting the geometry and coordinate axes. (b) Definition of cross sections along the long axis that are used in the text.

terms taken into account are the exchange, demagnetizing, and Zeeman (externally applied field) energies. Magneto-crystalline anisotropy and thermal fluctuations are neglected throughout this work. Within the continuum formulation, the exchange energy can be written as¹¹

$$E_{ex} = - \int_V A \mathbf{m} \cdot \left(\frac{\partial^2 \mathbf{m}}{\partial x^2} + \frac{\partial^2 \mathbf{m}}{\partial y^2} + \frac{\partial^2 \mathbf{m}}{\partial z^2} \right) dV, \quad (1)$$

where V is the sample volume, A the exchange stiffness constant, and $\mathbf{m} = \mathbf{M}/M_s$. The demagnetizing energy is expressed as¹²

$$E_d = - \frac{\mu_0}{2} \int_V \mathbf{H}_d \cdot \mathbf{M} dV, \quad (2)$$

in which μ_0 is the magnetic permeability in vacuum and \mathbf{H}_d is the demagnetizing field. Finally, the Zeeman energy is evaluated as

$$E_Z = - \mu_0 \int_V \mathbf{H}_A \cdot \mathbf{M} dV, \quad (3)$$

where \mathbf{H}_A is the externally applied magnetic field. From the total energy density, $E_{tot}/V = (E_{ex} + E_d + E_Z)/V$, the associated effective field term acting on \mathbf{M} can be calculated from $\mathbf{H}_{eff} = -\mu_0^{-1} V^{-1} \partial E_{tot} / \partial \mathbf{M}$. The effective field is then comprised of the exchange, demagnetizing and applied fields; $\mathbf{H}_{eff} = \mathbf{H}_{ex} + \mathbf{H}_d + \mathbf{H}_A$. In effect, the exchange field is written as $\mathbf{H}_{ex} = \frac{2A}{\mu_0 M_s^2} \nabla^2 \mathbf{M}$ and the applied field is simply \mathbf{H}_A . The demagnetizing field is expressed as $\mathbf{H}_d = -\hat{N}\mathbf{M}$, where \hat{N} is the demagnetization tensor, whose elements are evaluated analytically following the derivations of Newell *et al.*¹³ To calculate the time dependence of \mathbf{M} , we solve the Landau-Lifshitz (LL) equation of motion,^{12,14}

$$(1 + \alpha^2) \frac{\partial \mathbf{M}}{\partial t} = - \gamma_0 [\mathbf{M} \times \mathbf{H}_{eff}] - \frac{\alpha \gamma_0}{M_s} \{ \mathbf{M} \times [\mathbf{M} \times \mathbf{H}_{eff}] \}, \quad (4)$$

where α is a phenomenological damping parameter, t the time, and γ_0 the gyromagnetic ratio (2.21×10^5 m/A s used here). The first term on the right-hand side of Eq. (4) describes the precession of \mathbf{M} around \mathbf{H}_{eff} and the second term is the dissipation providing a relaxation directed toward \mathbf{H}_{eff} . The equilibrium condition for a given distribution of \mathbf{M} is $\mathbf{M} \times \mathbf{H}_{eff} = 0$. In order to simulate the system, the continuum

representation has to be discretized. In this work we consider a stripe of length $L = 1536$ nm, width $w = 75$ nm, and thickness $t = 9$ nm. We employ a finite-difference scheme, whereby the continuum is discretized into a spatially invariant mesh with cells having dimensions $(\Delta x, \Delta y, \Delta z) = (3 \times 1.5 \times 9 \text{ nm}^3)$, i.e., $512 \times 50 \times 1 = 25$ 600 cells. Each cell is represented by a magnetization vector \mathbf{M} . The second derivatives in the expression for \mathbf{H}_{ex} is approximated by a three-point stencil in each spatial direction, e.g., $\frac{\partial^2 \mathbf{m}(\mathbf{r})}{\partial x^2} = \frac{1}{\Delta_x^2} [\mathbf{m}(\mathbf{r} + \Delta_x \hat{x}) - 2\mathbf{m}(\mathbf{r}) + \mathbf{m}(\mathbf{r} - \Delta_x \hat{x})]$ and similarly for the y and z derivatives. The demagnetizing field at a point \mathbf{r}_i due to dipoles at points \mathbf{r}_j is expressed as $\mathbf{H}_d^i = -\sum_j \hat{N}(\mathbf{r}_i - \mathbf{r}_j, \Delta x, \Delta y, \Delta z) \mathbf{M}_j$. Due to the form of this expression, fast Fourier transform (FFT) techniques are used for its evaluation.^{15,16} The LL equation [Eq. (4)] is numerically integrated using a fifth-order Runge-Kutta scheme with Cash-Karp coefficients.¹⁶⁻¹⁸ In this work, material parameters typical for permalloy are used with $A = 13$ pJ/m and $M_s = 800$ kA/m. To trap a 360° DW in the stripe, the magnetization vectors (\mathbf{M} 's) are initialized to a configuration close to the desired DW structure and the system is let to relax toward equilibrium with a high damping coefficient $\alpha = 0.9$ and adaptive time stepping in order to reach convergence quickly. The system is considered to be in equilibrium when $\frac{1}{M_s^2} |\mathbf{M} \times \mathbf{H}_{eff}| \leq 10^{-6}$ in each cell. In order to calculate and visualize spin-wave modes, the system is first perturbed with a 5 Oe field, \mathbf{h}_p , along $+x$ and let to reach equilibrium, using the same α and equilibrium condition as when creating the initial DW configuration. Then, setting $\mathbf{h}_p = \mathbf{0}$, $\alpha = 0.01$ and a constant integration time step $\Delta t \approx 5.66 \times 10^{-14}$ s, the free oscillation ringdown of \mathbf{M} in each cell is recorded, sampling every 2.26 ps. Local FFT power spectra are computed for each cell and then summed over all \mathbf{r}_i to obtain a total spectrum; $\bar{P}_z = \sum_i |\sum_j m_z(\mathbf{r}_i, t_j) e^{i2\pi f t_j}|^2$.¹⁹ Images of the spatial variation in oscillation power corresponding to the resonance peaks of interest in the total spectrum are then selected and visualized. An identical procedure is then followed for a 5 Oe perturbation \mathbf{h}_p along $+y$. For the case of resonant driving of the system, we select the frequency of interest and apply a global Zeeman term varying in time as $H_A = h_{rf} = H_0 \sin(2\pi f t)$, where H_0 is the field amplitude (applied either along x , or y), f is the frequency, and t is the time.

III. RESULTS AND DISCUSSION

For the characterization of the normal modes, we shall first need to study the equilibrium magnetization and effective field distributions. Figure 2(a) shows a color plot of the relaxed static magnetization distribution of the entire stripe, a blown-up region around the 360° DW (with characteristic regions marked I-V) while (b) shows the corresponding vector plot. Here, regions I and V should be understood to exclude the edge domains (EDs). The 360° DW in Figs. 2(a) and 2(b) may be thought of as a composite object comprised of two distorted coupled TDWs of opposite polarity. We will henceforth denote the constituent TDWs as y -domains; $+y$ -domain for an in-plane magnetic polarization along $+y$ (region II in the figure) and $-y$ -domain for a magnetization

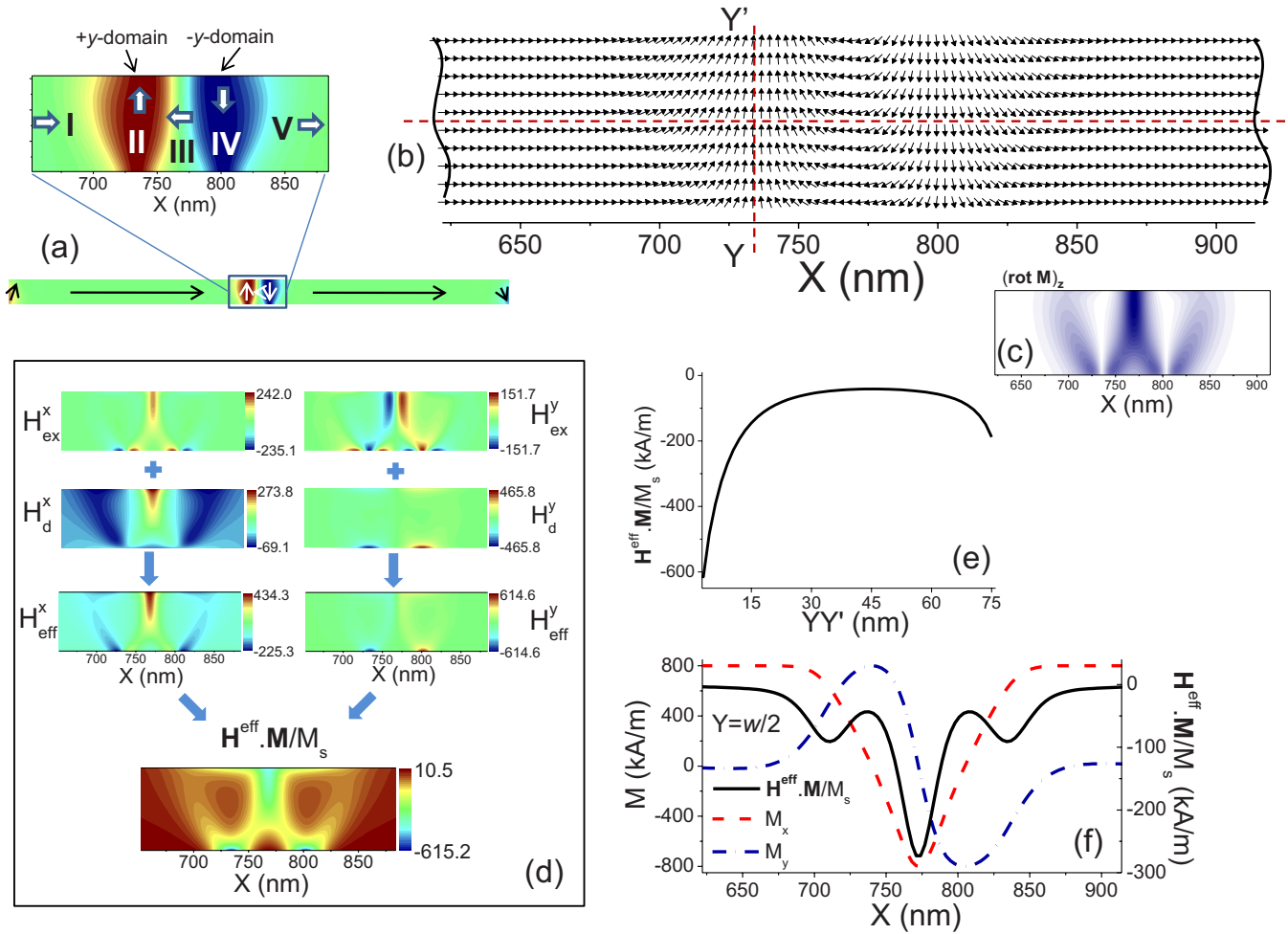


FIG. 2. (Color online) (a) The static magnetization distribution of the entire sample (y component) with arrows indicating the local magnetization directions and a blow-up region with characteristic areas marked I-V. (b) Vector plot of the magnetization distribution (not all vectors shown). (c) $\text{abs}[(\text{rot}\mathbf{M})_z]$. (d) x and y components of the exchange field H_{ex}^x , H_{ex}^y , demagnetizing field H_d^x , H_d^y , the effective field H_{eff}^x , H_{eff}^y and $\mathbf{H}_{\text{eff}} \cdot \mathbf{M}/M_s$ all with data scales in units of kiloampere per meter. (e) $\mathbf{H}_{\text{eff}} \cdot \mathbf{M}/M_s$ on the cross-section YY' as defined in (b). (f) M_x , M_y , and $\mathbf{H}_{\text{eff}} \cdot \mathbf{M}/M_s$ on $Y=w/2$ [dashed horizontal line in (b)].

along $-y$ (region IV in the figure). The 360° DW is a head to tail DW, in this case with a magnetization along $+x$ on the left (region I) and right (region V) sides of the 360° DW. The separating area (region III) between the y -domains has an average magnetization along $-x$. These characteristics lead to the expectation of at least two basic in-plane dynamical behaviors when driving the system with small in-plane fields along either x or y ; applying a small field along $+x$ should initially compress the y -domains (letting region I and V grow at the expense of III), while a field along $-x$ should move the y -domains further apart (expanding region III). Therefore, one behavior should be an in-phase oscillatory translational motion of the y -domains along x . Further, if the perturbation is applied along $+y$, the $+y$ -domain will expand while the $-y$ -domain will shrink and vice versa for a field applied along $-y$. Therefore, another expected behavior is out-of-phase breathing of the y -domains (i.e., when one y -domain is expanded the other one is contracted). We will later also see wobbling, i.e., periodic tilting motions of the y -domains.

As we considered some expected vibrational behaviors of the 360° DW as a whole, viewed in terms of a DW of the

stripe, we must now consider the DWs “substructure.” These are the Neel walls surrounding the y -domains. In order to guide the eyes in visualizing the spatial extension of these, we have plotted $\text{abs}[(\text{rot}\mathbf{M})_z] = |\{\partial M_y / \partial x - \partial M_x / \partial y\}z|$ in Fig. 2(c), whereby a high intensity of blue color indicates the presence of a DW.^{20,21} In the text, we shall at times refer to the DWs of the substructure in terms of the characteristic regions marked in Fig. 2(a). From now on when we speak about a DW we shall refer to the (I-II), (II-III), (III-IV), and (IV-V) transient regions as DWs and the domains are the y -domains and the (III) domain. Whenever we talk about the composite object we shall refer to it as the 360° DW. From Fig. 2(c) we see that the spatial inhomogeneity of the DW cores are significantly large. Next, we need to address the spatial distribution of \mathbf{H}_{eff} which is generated by this equilibrium magnetization distribution. From other works, it is known that spin excitations may be trapped and/or scattered in narrow regions of inhomogeneities of the effective field, thus causing localized modes in the DW cores and at edges²²⁻³³ or imposing a confining boundary leading to SW quantizations, similar to geometrical confinement.^{25,34} The

computed effective field is shown in Fig. 2(d) as the (x, y) components of the exchange, demagnetizing, and effective (exchange+demagnetizing) fields at equilibrium. To create a map of the field inhomogeneities, we plot the total field generated by the equilibrium magnetization, $\mathbf{H}_{\text{eff}}^{\text{tot}}$ as $\mathbf{H}_{\text{eff}}^{\text{tot}} \cdot \mathbf{M} / M_s$.²⁵ We can see from the constituent components of $\mathbf{H}_{\text{eff}}^{\text{tot}}$ that there are two contributions to narrow dips in the field profile; the DW cores as described above and the top and bottom of the y -domains where there are free poles, yielding narrow wells due to large demagnetizing fields. This is clearly shown in the line plots, taken at different cross sections of the structure. Figure 2(e) shows $\mathbf{H}_{\text{eff}}^{\text{tot}}$ along the section YY' defined in Fig. 2(b). It is comprised almost exclusively by the large demagnetizing fields generated by the magnetic charges at the lateral edge. Furthermore, it is asymmetric along YY' . Figure 2(f) shows a cross section of $\mathbf{H}_{\text{eff}}^{\text{tot}}$ along $Y=w/2$, with a narrow dip as M_y changes sign (over region III). The two shallower side dips stem from the (I-II) and (IV-V) DWs. As found in previous work on multidomain particles, first, the DWs may act as confinements for SWs, causing highly localized resonances,^{25,35,36} giving rise to DW modes.²⁵ The same occurs at edges, where there are large gradients in the demagnetizing field, being here the regions at the top and bottom of the y -domains. Second, higher-frequency modes can occur within the domains, in our case the y -domains and III-domain, in regions with much smaller gradients in the effective field distribution, whereby quasi-uniform modes and higher-order quantized spin-wave modes occur.^{25,35,36} Within the set of domain modes, there may be quantization with nodal lines parallel or perpendicular to the magnetization vectors, i.e., Damon-Eschbach (DE) or backward (BA) types, respectively. Their quantization may then consist of two boundaries within a domain; (i) the geometrical ones on $L=(0, w)$ imposing quantization along y and (ii) the surrounding DWs, imposing quantization along x ; When a SW hits a DW, it will be partly reflected and partly transmitted. The reflectivity (and induced phase shift) indeed depends (among other things) strongly on the wave vector and thus the wavelength of the incoming SW.³⁷ In fact, a critical parameter is the SW wavelength in comparison to the DW width.³⁷ The degree of the DWs confinement effects varies with frequency.

In general, complications will arise when (i) the DW core profile (shape and/or depth) varies significantly with position and (ii) when dynamical dipolar coupling between different modes is significant. Consequences of (i) may be expected to give rise to a distribution of oscillations over a range of modes in different parts of the structure. An example of this can, for instance, be found in Ref. 26 whereby within the DWs of a Landau state particle, the corners (which are part of the DW) exhibit some different modes than the rest of the diagonal parts. In addition, the SW reflectivity of the DW should also vary with position if the DW width varies significantly, giving rise to very complex reflectances and DW confinement effects. The type of couplings in (ii) include dynamical dipole coupling between DW modes and the SW modes of the domains, DW-DW coupling, coupling of the modes on the top and bottom of the y -domains to each other and/or to DWs and domains and domain-domain coupling. The first of these, i.e., DW and domain SW-mode hybridiza-

tion was highlighted in Ref. 25 for the case of a permalloy square in the Landau state, whereby composite absorption peaks in their measurements were, based on micromagnetic simulations and analytical calculations, attributed to coupling between domain SW modes and fundamental vibration modes of a DW. In our structure, we will initially expect SW-mode localization at the lateral edges (where the y -domains generate large demagnetizing fields) and within the (I-II), (II-III), (III-IV), and (IV-V) DWs. Further, in regions with a higher degree of effective field homogeneity away from the edges in the y -domains, we expect to excite quasiuniform-type domain modes and higher order multimodal BA and DE SW modes.

In this work, resonances are excited by uniform in-plane magnetic fields along the x and y directions. The modes that will be excited are sensitive to the relative orientation of their magnetization distribution and the excitation direction, i.e., to the symmetry of the exciting torque.³⁸ Regions where $\mathbf{h}_p \times \mathbf{M} \neq 0$ are where the perturbation will couple to. In effect, the results here represent a limited set of possible modes. The total power spectra for perturbations along x and y are shown in Figs. 3(a) and 3(b) (blue lines), respectively. In addition, for comparison purposes, the corresponding calculations for the case of the stripe without the 360° DW (red dashed lines) have been carried out.

We will now discuss the cases corresponding to modes excited by a perturbation $\mathbf{h}_p \parallel x$ (case I) and $\mathbf{h}_p \parallel y$ (case II). In the last section we shall drive the system at the frequencies of the highest intensity peaks for each of these cases and analyze their behavior.

A. Case I: $\mathbf{h}_p \parallel x$

Figure 3(a) shows a limited section of the total FFT power spectrum for case I with images of the FFT power spatial distribution at some selected frequencies. The blue solid line (with DW) corresponds to the stripe containing a 360° DW and the red dashed line (no DW) corresponds to the stripe without the 360° . Spin-wave modes that have their maximum FFT power in the stripe's edge regions (as $x \rightarrow 0$ and $x \rightarrow L$) are denoted EM(n), i.e., edge modes, where n is the number of nodes. All other selected peaks are named α , β , \dots , η and correspond to spin-wave modes that appear to exist due to the presence of the 360° DW. The spatial distribution of the FFT power of each indexed peak is in Fig. 3 plotted in the region of interest, i.e., either the 360° DW or ED region. For this excitation geometry there is no coupling to regions I and V since $\mathbf{h}_p \times \mathbf{M} = 0$. We expect coupling to the y -domains, the DWs around them and the EDs and, observations of traveling SWs in I and V should stem from ones radiated by the 360° DW and/or EDs. As an example of SW radiation from the 360° DW, we have plotted the FFT power within the entire stripe for the δ mode (11.22 GHz). These SWs travel and interfere. Therefore, above the forbidden traveling SW frequency gap of the stripe, the standing wave pattern formed by them also contributes to the spectrum. EMs are not the object of this paper but we include them in the spatial FFT plots for completeness. Due to the shape of the EDs, the corresponding oscillation power distri-

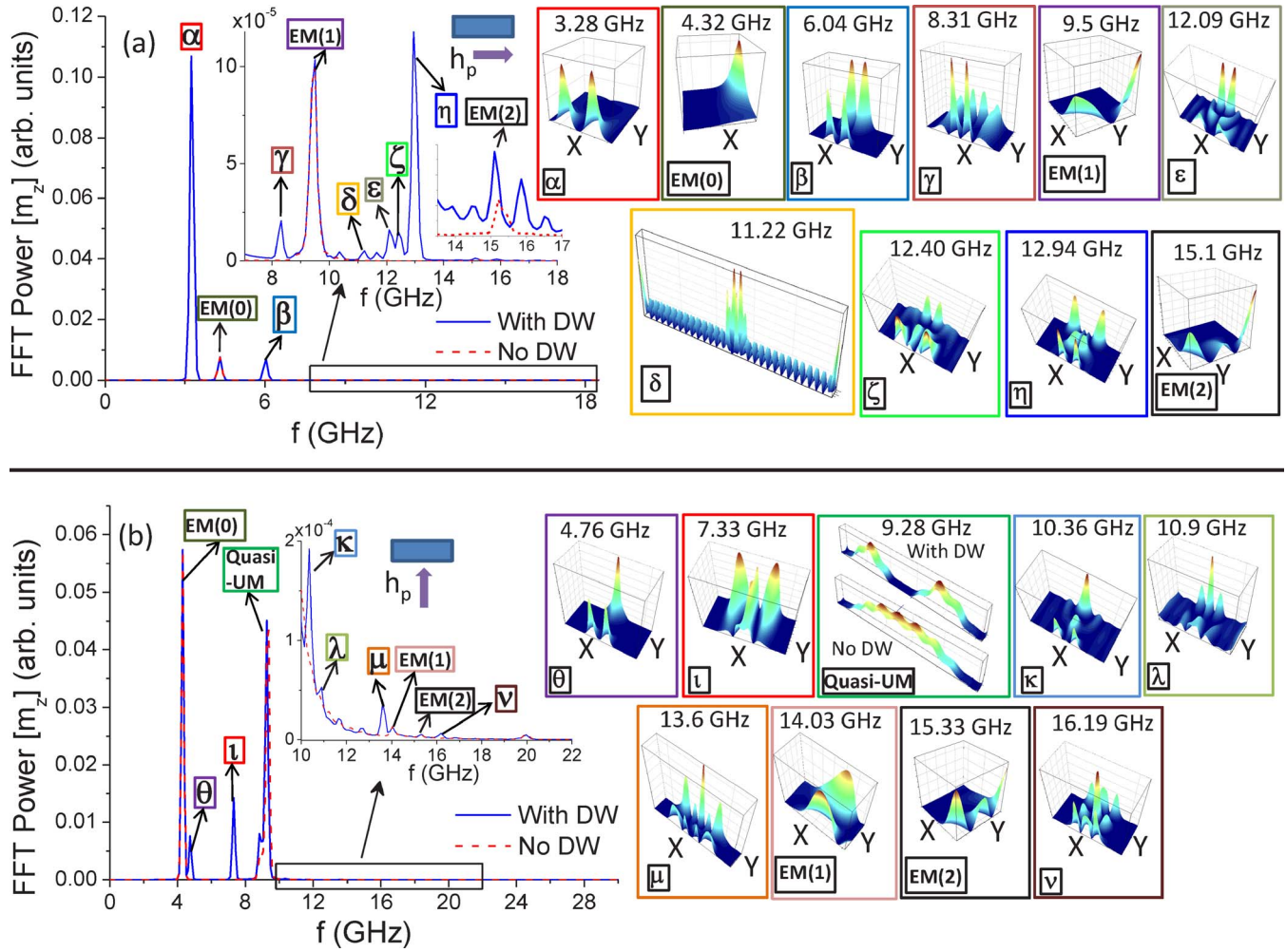


FIG. 3. (Color online) (a) Total FFT spectrum for the case where $\mathbf{h}_p \parallel x$. Peaks indexed α - η correspond to modes with dominant FFT power within the DW regions. EM(n) means power concentrated to the stripe edges, with n being the number of nodes. The spatial distributions of the FFT power are shown as 3D maps within the region of interest, i.e., for α - η the spatial plots are within the DW area and for EM(n) modes, the data is plotted close to the stripe edge (as $x \rightarrow 0$ and $x \rightarrow L$). (b) As in (a) but for the case $\mathbf{h}_p \parallel y$. Here, UM stands for uniform mode.

Contributions are not spatially symmetric as can be seen for EM(0)(4.32 GHz), EM(1)(9.5 GHz), and EM(2)(15.1 GHz). One thing worth mentioning however, is a noticeable frequency shift, $\Delta f \approx 200$ MHz of the EM(2)-peak between the cases “With DW” and “No DW,” which is not observed for EM(0) and EM(1) (see the inset in the total spectrum). The image of the spatial FFT power for EM(2) was plotted here for the case With DW. EM(0) cannot emit SWs that traverse the whole stripe since its frequency lies deep within the forbidden band gap. EM(1) can however, but no substantial frequency shift is seen (the blue and red lines coincide well). We can also exclude the possibility of the relative frequency shift between the two cases to be the result of a 360° DW normal mode occurring close to the frequency of the EM(2) because looking at the FFT power throughout the stripe, the oscillation power is always dominantly concentrated to the ends (not shown here) and is actually weakest across the 360° DW. The reason for the observed Δf is likely to result from SW interactions with the 360° DW which we will later see is the reasonable cause.

Let us now consider peaks pertaining to the presence of the 360° DW. A more detailed view of FFT-power distributions is shown in Fig. 4. We notice from Fig. 3(a), that α and β have much more power than other modes. These oscillations are concentrated to the lateral edges of the stripe corresponding to the top and bottom of the y -domains where there are surface charges and consequently large demagnetizing fields. Thus, we can directly correlate them to the $\mathbf{H}_{\text{eff}}^{\text{tot}}$ profile in Fig. 2(e) with strong concentration of FFT power in the deep extrema of $\mathbf{H}_{\text{eff}}^{\text{tot}}$ (or rather \mathbf{H}_d^y which is dominating on this cross section). Cross-sectional line plots along y through the maxima of the FFT power and H_y^{eff} are shown in Figs. 4(a) and 4(b). In addition, from the FFT data, we find that the phase (not shown here) between the maxima for α are π out-of-phase, so that taken on a cross section $Y=0$ the mode profile is antisymmetric. In fact, we find no other peak corresponding to a symmetrical α mode implying that the two oscillating components are strongly dipole coupled. Similarly, phase data for β shows that the maxima on $Y=0$ are π out-of-phase with respect to each other and similarly

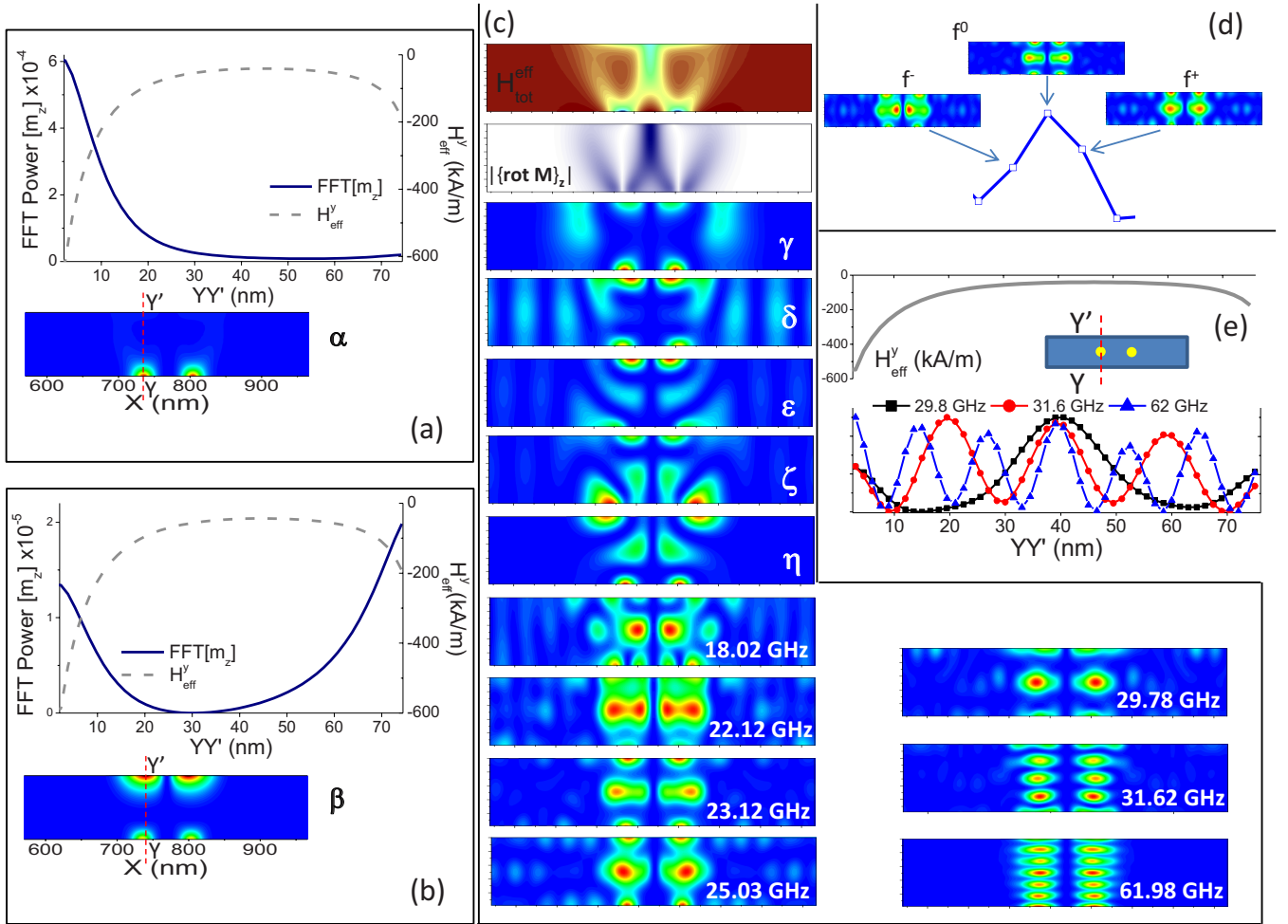


FIG. 4. (Color online) (a) The spatial distribution of the FFT power for the α resonance with a line plot of the FFT power and H_{eff}^y along a cross-section YY' running through the point of maximum FFT power on $Y=0$ (indicated by the red dotted line). (b) As in (a) but for β with the cross section running through a maximum on $Y=w$. (c) Spatial FFT-power distribution maps around the 360° DW for different modes discussed in the text along with $\text{abs}\{\{\text{rot} \mathbf{M}\}_z\}$ and $\mathbf{H}_{\text{tot}}^{\text{eff}}$ maps. Note that the spatial FFT plots have different data scales and the intensities cannot be directly compared. (d) Sampling of the spectral composition of a peak at 23.12 GHz discussed in the text. (e) FFT-power line profiles for the three domain modes in (c), each normalized to their respective maximum value.

on $Y=w$ and that the oscillatory components are in-phase across the diagonal reflection line connecting the maxima [see also Figs. 9(g) and 9(h)]. If, for a moment we consider each y -domain separately, α and β compare quite well to modes reported on for onion-state ring structures, where TDWs constituted the DWs defining the onion state.^{29,30} α and β are therefore analogous to what they termed outer/inner EMs. It is noticed that the FFT power is actually non-zero on the whole cross section and we cannot call them strictly edge localized in that sense. In Fig. 4(c) we have summarized the FFT-power distribution around the 360° DW for peaks γ - η and a selection of other high-frequency patterns along with the $\text{abs}\{\{\text{rot} \mathbf{M}\}_z\}$ and $\mathbf{H}_{\text{tot}}^{\text{eff}}$ maps. Note that with the current perturbation direction, we do not couple to the central parts of region III. Regions of coupling are therefore to the (I-II), (II-III), (III-IV), and (IV-V) DWs and in the y -domains (and EDs). Let us start by observing γ - η . These appear to be present in different parts of the (I-II), (II-III), (III-IV), and (IV-V) DWs. Interestingly, such scattered modes in the DWs were not reported in the works of the

TDWs in onion-state rings.^{29,30} Looking at the $\mathbf{H}_{\text{tot}}^{\text{eff}}$ and $\text{abs}\{\{\text{rot} \mathbf{M}\}_z\}$ maps, all of our DWs are spatially highly inhomogeneous. Therefore, it is reasonable that we observe oscillations distributed over a range of modes located in different parts of the DWs. Further, due to the proximity of these DWs with respect to each other, we cannot exclude dynamical dipolar coupling between them. As pointed out by Bailleul *et al.*,²⁵ many of the resonance peaks can be of composite nature, such that, when we index a peak at its maximum point and display the corresponding FFT-power distribution, this may be made up of several other modes. This would indicate intermode coupling. What was found in Ref. 25 was coupling between the vibrational DW modes and the SW modes of the domains. In their case, the DWs were well separated and inter-DW couplings could be neglected. This is however not necessarily the case here and it is not clear how to separate the different coupling effects for our case with spatially inhomogeneous DWs. It should be noted that ϵ - η exhibit some spreading into the y -domains. It is therefore possible that this is an effect of a coupling between DW and

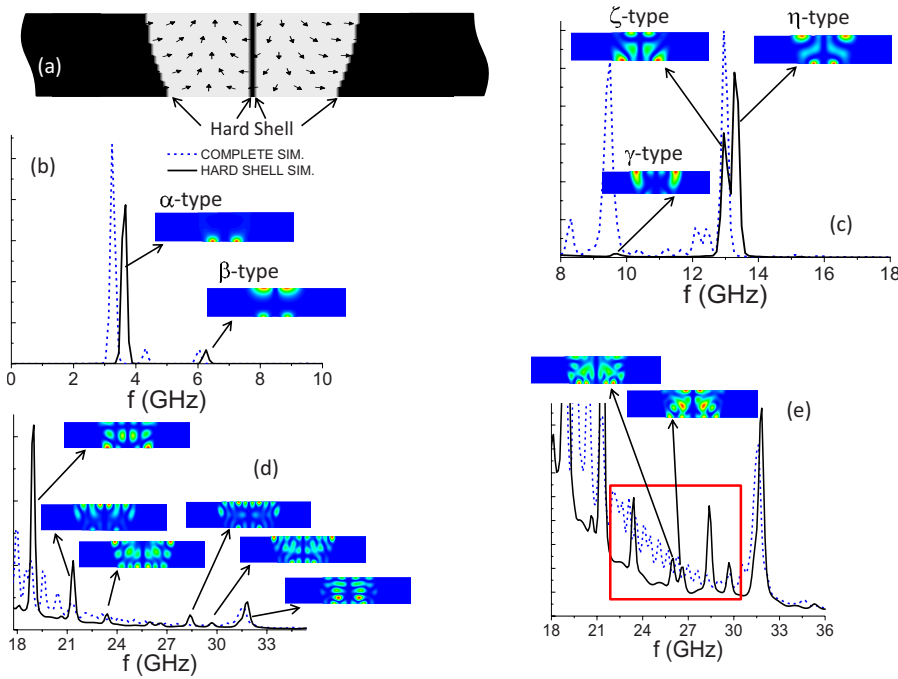


FIG. 5. (Color online) (a) The shape of the hard shell, whereby the equations of motion are solved within the gray regions. Black areas are dynamically still. (b)–(e) different parts of the resulting spectrum from the hard shell simulations, discussed in detail in the text. Black lines are the “hard shell case” and blue dashed lines correspond to the original simulation. The red rectangle in (e) highlights the frequency region where the original simulation shows a broad region with tightly spaced peaks.

domain modes. At frequencies above η , oscillations with a high degree of spreading within the y -domains are observed. We therefore make a distinction to call the modes found above η as (y) domain modes. A small selection is shown within the interval 18.02–61.98 GHz, where we find the quasiuniform mode of the y -domains and multinodal quantized SW modes of BA-type (see 25.03–61.98 GHz). These are analogous to domain modes in TDWs in rings,³⁰ here with the difference that in this structure we have a non-negligible dipolar coupling between the y -domains. At these higher frequencies, there appears to be many variations in domain modes such as those shown at 18.02, 23.12, and 25.03 GHz. In fact, there is a wide frequency interval (20–31 GHz), where a large number of varieties of domain modes are found and the spectrum is broad with many tightly spaced peaks [see the blue dashed line in Fig. 5(e)], similar to the ones shown at 18.02, 22.12, 23.12, and 25.03 GHz (but with variations in the location within the y -domain of the global FFT maxima). Embedded in this region are also other n -node BA domain modes (not shown here). Then at 31.62 GHz (spatial plot shown in figure), this broad region is interrupted by a clear peak approximately ten times higher in amplitude. We also checked the composition of the spectral peaks and show a sample of this in Fig. 4(d) where the peak maximum is at 23.12 GHz (f^0) and two points within the linewidth at approximately ± 100 MHz, f^+ and f^- , respectively, are sampled. Note the differences in the location of the global FFT maxima within the y -domains. This should not be a numerical artifact since as we stated, at 31.68 GHz, a clear peak, approximately ten times higher in amplitude than the peaks in the broad distribution just described, appears with a “clean” multinodal structure. It should be noted that at lower frequencies (≤ 18 GHz), the peak composition is more homogeneous and well defined, i.e., the spatial distributions of the oscillations do not vary much within the linewidth of the resonance peaks. One possibility is, that at higher frequen-

cies, the occurrence of a smearing in the resonance spectrum, where there is a large set of domainlike modes spaced very tightly in frequency are the results of strong coupling of both quasiuniform and multinodal domain modes to the DWs and in addition interdomain coupling (here coupling of the domain modes in the $+y$ and $-y$ domains). In addition, it is possible that at these SW wavelengths the confinement conditions imposed by the DWs result in more complicated resultant patterns. We have therefore, in general, several effects that may contribute to the observed phenomena; (i) effects of SW confinement by DWs, (ii) dynamic dipolar coupling between DW and domain modes, (iii) inter-DW coupling, (iv) intercoupling of the lateral edges (top and bottom of the y -domains and in turn coupling of them to DW and domain modes), and (v) influence of generated SWs that have traveled out from the y -domains, been reflected at the EDs and/or physical edges and then returned back (including associated phase shifts) as well as radiated SW from the EDs. A separation of all of these is however not possible within the data collected for these simulations and apart from the work in Ref. 25 dealing with more homogeneous DW cores and domain magnetizations, we do not know of any analytical work dealing with highly inhomogeneous DWs that may be applicable to our case. However, certain (qualitative) information may be obtained regarding points (i) and (v) here; Let us initially uncouple (i) and (v); For confining boundaries imposed by the DWs surrounding the y -domains one may expect to see SW quantization along x , i.e., DE modes. In the frequency region (18–31 GHz) we see the tendency toward such effects [see, e.g., 22.12 and 23.12 GHz in Fig. 4(c)]. The example shown at 18.02 GHz also indicates the simultaneous occurrence of BA and DE modes. We are interested in acquiring information regarding the degree of DW induced SW confinement along x and how this may affect the spectrum in the diffuse region 18–32 GHz. It is instructive to consider a case of perfectly reflecting DWs and

in addition suppress any incoming SWs from regions I and V. If we indeed have strong reflectances from the DWs we may expect to find some similarities to the artificial case of perfect reflection. In a rough calculation, we therefore imposed the extreme case of “hard boundaries” around the y -domains, meaning a SW reflectivity of unity. In so doing, we must take care to retain the magnetization distribution and dipolar couplings in the y -domains. In order to put a “hard shell” around the y -domains, we fixed the \mathbf{M} 's in locations where $m_x \geq 0.999$ and along two computational cells in between the y -domains. The latter was assumed to be reasonable due to the observation that this region appears to be more or less dynamically inactive, judging from the spatial FFT-power plots. The resulting dynamically active region is shown in gray color in Fig. 5(a). Black color here means regions where \mathbf{M} are fixed and where Eq. (4) is not solved. All dipolar and exchange couplings are retained between the active and fixed regions in order to keep the same initial magnetization distribution within a y -domain. The system is then perturbed with $\mathbf{h}_p \parallel x$ as before [but coupling only now to the gray areas in Fig. 5(a)] and then let to relax. The resulting total FFT-power spectrum is summarized in Figs. 5(b)–5(e). The α and β modes are recovered at low frequencies but shifted to slightly higher frequencies [Fig. 5(b)]. In Fig. 5(c), we see that also γ , ζ , and η are more or less present as well, again shifted toward higher frequencies. However, the ϵ and δ modes are completely suppressed. Now, in imposing a hard shell, we expect to have slightly suppressed translational, wobbling, and breathing of the whole y -domains which are expected to occur, as we discussed previously in the text (and that we shall see explicit examples of in the last sections when we continuously drive the system). The system is in that sense “stiffer,” which may explain the shifting of the observed low-frequency modes to slightly higher frequencies. In total, within the region of DW modes we reproduce the main modes quite well. The reason for the absence of ϵ and δ cannot be resolved for certain by this simulation since we have eliminated traveling SWs from other parts of the stripe. We will estimate their effects later on in the text. We now turn to the domain modes in Figs. 5(d) and 5(e). Here, we find the expected clear mixture of DE and BA modes due to two-dimensional (2D) confinement. Notice also that the multinodal BA mode at 31.6 GHz coincides with the first simulation. We may now compare the broad region (18–32 GHz) in the original simulation to this one. A noticeable similarity between the mode at 18.02 GHz in Fig. 4(c) and the one at ≈ 19 GHz in Fig. 5(d) is noticed. At other frequencies there are much more DE influences on the modes than in the original simulation. In general, one notices a more well defined clear spectrum corresponding to the hard shell simulation; Fig. 5(e). Since we know from the hard shell calculation that the y -domains are likely to sustain a large population of n -BA \times m -DE modes for highly reflecting boundaries, the lack of them in the original simulation suggests (but not proves) that the DWs in this frequency interval imposes relatively weak confining boundaries along x for SWs.

In the hard shell simulations, we have cut off any influences induced by the SWs coming from other parts of the stripe [point (v)]. These will now be investigated and the

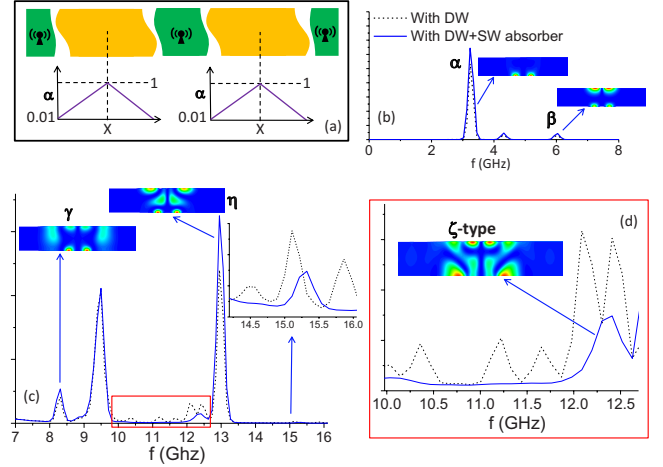


FIG. 6. (Color online) (a) Schematic of the setup for using SW absorbers. Green color are areas where there are domain walls that radiate SWs and orange color is where the damping is linearly varied according to the graphs below. (b)–(d) Different parts of the spectrum using SW absorbers. Blue solid lines correspond to the case with the absorbers and black dashed lines to the original simulation.

results cross checked with the previous results; For the following simulation, the hard shell is turned off in order to turn any DW quasiconfinement effects back on and SW absorbers are artificially placed between the y -domains and EDs. This is schematically shown in Fig. 6(a). The idea is as follows; since we do not couple to regions I and V by this perturbation, SWs should be emitted from both sides of the y -domains and from the EDs. We therefore put regions with varying damping in between to absorb the SWs, thus preventing them to be reflected and to travel back into the y -domains, as well as absorbing SWs radiating from the EDs flowing directly toward the 360° DW. The damping is varied linearly from 0.01–1 and from 1–0.01 within the absorbing areas [see Fig. 6(a)]. The simulation procedure and data processing are performed in the identical manner as previously. The result is shown in Figs. 6(b)–6(d). In Fig. 6(b), α and β are found completely overlapping with the original simulation as well as EM(0). Also, γ and η are fully recovered [Fig. 6(c)]. However, some changes are noticed between 10 and 12.5 GHz as shown in Fig. 6(d). Several peaks from the original simulation are in this case suppressed and the ϵ and δ modes are not present. Instead we find only a ζ -looking mode at ≈ 12.35 GHz. In fact, observing it closely, it contains elements of ϵ and δ . This is a clear indication of the effects of interference from traveling SWs that are present without SW absorbers. The effect then of such SWs here is splittings of DW modes into a set of its constituent components. It is now also apparent that the suppression of ϵ and δ in the hard-shell simulation is unlikely to be due to confinement effects along x but rather to the absence of interfering reflected SWs. With respect to the diffuse region 18–32 GHz, using SW absorbers do not affect its appearance, i.e., it remains as a broad region containing many tightly spaced peaks such as the blue dashed line in Fig. 5(e). The reason for its appearance is therefore likely to stem predominantly from dynamical dipolar coupling between domain and DW

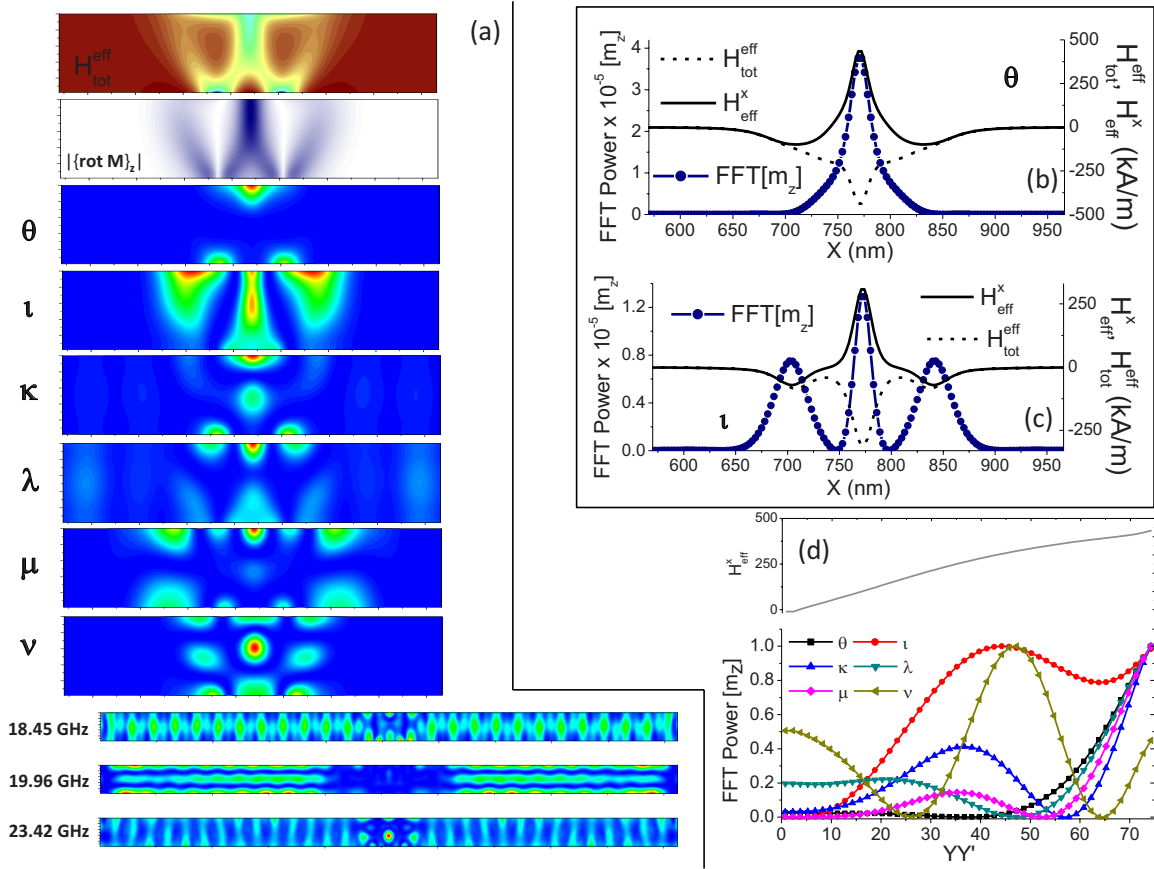


FIG. 7. (Color online) (a) The spatial distribution of FFT power for the discussed modes along with $\text{abs}(\{\mathbf{rotM}\}_z)$ and $\mathbf{H}_{\text{tot}}^{\text{eff}}$ as well as examples of plots of the entire stripe showing SWs traversing the whole geometry. (b) Line plots of the FFT-power profile along x on $Y = w$ for θ along with the pertinent effective field component showing that H_{eff}^x dominates. (c) As in (b) but for l and along a cross section along x running through the point of maximum FFT power in the (III) domain. (d) Effective field and FFT-power profiles taken along y along the center of the (III) domain, each curve having been normalized to its respective maximum value.

oscillations (both within each y -domain but possibly also coupling between one y -domain to the other).

B. Case II: $\mathbf{h}_p \parallel \mathbf{y}$

A section of the corresponding spectrum for this case is shown in Fig. 3(b) having indexed peaks θ - ν and with the corresponding spatial FFT-power distributions shown beside. A more detailed plot is given in Fig. 7 along with the $\mathbf{H}_{\text{tot}}^{\text{eff}}$ and $\text{abs}(\{\mathbf{rotM}\}_z)$ maps (all plots are made around the 360° DW region). The first peak [EM(0) in Fig. 3(b)] is the same EM observed in case I with the same spatial FFT-power distribution and is therefore not shown here. In contrast to the previous case, we will here couple strongly to the center of region III and negligibly to the y -domains. Further, similarly to case I resonances will be excited in all of the surrounding DWs. An additional complication arises here, because \mathbf{h}_p couples ideally to region I and V. Therefore, we will always excite SWs from the homogeneously magnetized parts of the stripes which can travel into the 360° DW and interact. Three selective plots of the oscillation power throughout the whole stripe are shown at the bottom of Fig. 7(b) (18.45, 19.96, and 23.42 GHz) to illustrate this. Therefore, for frequencies above the SW band gap it is to be understood that the spec-

tral power includes SWs stemming from regions I and V. At 9.27 GHz, we excite the quasiuniform mode of the entire stripe. Notice that the presence of the 360° DW divided the quasiuniform mode into two parts. Further, on top of the mode there is a ripplelike structure. As in previous works, we attribute this to a BA-type mode (in terms of the magnetization direction in regions I and V) having a similar frequency as that of the quasiuniform one and with $\alpha=0.01$ we are not able to resolve what should actually be two peaks.^{28,39} The indexed peaks in the shown part of the spectrum are ones where the FFT power is much higher in the 360° DW region than in other parts of the stripe. In Fig. 3(b), the two highest peaks stemming from the presence of the 360° DW are θ and l . From Fig. 7(a) the localization for θ can be seen to be on the top of region III (on $Y=w$) and on $Y=0$. The new feature here is on $Y=w$. We would however expect this from the $\mathbf{H}_{\text{tot}}^{\text{eff}}$ profile where there is a narrow well that acts as to confine SWs. Looking at Fig. 7(b), where line plots along x on a cross section $Y=w$ are shown, we see that this is so. For l , most of III is activated. The maxima on each side of III occurs in the region of the (I-II) and (IV-V) DWs. Cross-sectional plots in Fig. 7(c) illustrate this, taken through the maximum pertaining to the (III) domain. In general, we find oscillations localized in different parts of the surrounding

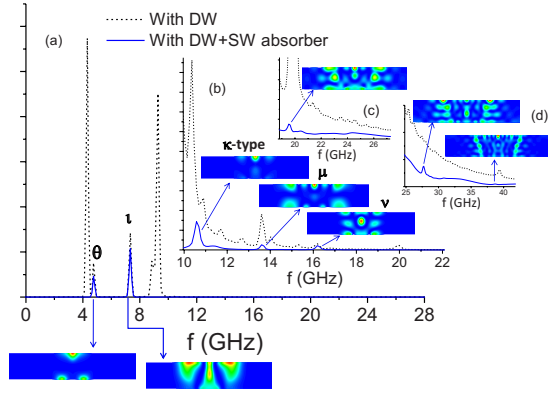


FIG. 8. (Color online) (a)–(d) Comparison plots in different parts of the spectrum for case II between the original simulation and that of using SW absorbers. Blue solid lines are with absorbers and black dashed lines correspond to the original simulation. The details are described in the text.

DWs as in case I. A feature of all the modes is the migration of maxima along y across III at various frequencies. In fact, we do not find any clear typical (III)-domain modes, such as m -DE types. Taking a section along the center of III along y and plotting $\mathbf{H}_x^{\text{eff}}$ (which is the dominating part of $\mathbf{H}_{\text{tot}}^{\text{eff}}$ there), we see that it has no flat parts but is rather a large gradient. The migration of the maxima therefore seems reasonable. This is shown in Fig. 7(d). Note that the FFT-power plots, there have been normalized to their respective maximum values for comparison purposes and therefore does not reflect their actual relation in intensity. Influences of inter-DW interactions etc., have been discussed in the previous paragraph (case I) and should also apply to case II. In an attempt to separate SW contributions from other parts of the stripe, we performed simulations with SW absorbers, similar to those in case I. However, some alterations in the procedure were made according to the following; the area, subject to the perturbation, was only that of regions where $m_x \leq 0.999$. This would correspond to the gray areas in Fig. 5(a) but also obviously including the two lines of computational cells along y in between the y -domains that had been removed in the previous case. In addition, the EDs were excluded from the perturbation. SW absorbers with a linearly increasing damping with distance was then put on each side of the y -domains. The result is shown in Figs. 8(a)–8(d). For the lowest frequency modes θ and ι , the spectra of the original simulation and this one agree perfectly, with the exception of the EM and the stripe’s quasiuniform modes since they are not excited. Differences are naturally observed above the SW propagation band gap [Figs. 8(b)–8(d)], where the spectrum now is much cleaner and we can more easily identify domain and DW modes pertaining only to the 360° DW structure. The μ and ν modes are the same as before while κ is slightly modified. λ is completely absent. Therefore, in the original simulations, the splitting of peaks resulting in distinct modes λ and κ are the result of interference from SWs originating from other parts of the stripe. At even higher frequencies, above 19 GHz, some unexpected observations are made. These are shown in Figs. 8(c) and 8(d), whereby multinodal modes apparently contained within the (I-II) and (IV-V)

DWs emerge. Although they may in some sense resemble vibrational DW modes, at such high frequencies we would rather call them domain like, where the (I-II) and (IV-V) DWs now could be considered to act as domains, with the y -domains then being the separating DWs. Further, they appear to impose quantization also along x and therefore resemble a 2D geometrically confined object.

C. Field-driven dynamics

In order to isolate and visualize the dynamical behavior of the 360° DW as a whole, we drive the system at some chosen frequencies. In the previous sections we have had to consider the 360° DW in terms of its constituent components. The aim of this section is to grasp an idea of its behavior at a larger length scale by stimulating it at frequencies extracted from the previous sections. We have chosen those corresponding to the highest intensity peaks in cases I and II; α , β , θ , and ι . The method of excitation has been described in Sec. II. The results of driving the system with a field $\mathbf{h}_{\text{rf}} \parallel x$ are summarized in Fig. 9, where (a)–(e) apply to 3.24 GHz (α) and (f)–(k) to 6.04 GHz (β). We wish in addition to the out-of-plane components also see the behavior of the y -domains. For full dynamical movies, we refer to the supplementary material.¹⁰ In order to obtain time snapshots of the dynamical magnetization for both m_y and m_z at their critical turning points on the oscillation curves we computed the time evolution of the volume averaged magnetizations in selected parts of the structure. Since m_x and m_z have a relative phase shift, we image them at various points in time. This is schematically shown in the inset in Figs. 9(a) and 9(f). Time snapshots of the spatial distribution of m_y and m_z were then taken at turning points on the oscillation curves. For the α mode we can see in Fig. 9(b) a predominantly translational and breathing behavior of the y -domains and out-of-phase oscillation for the m_z components on $Y=0$. A dynamical three-dimensional (3D) snapshot for m_z is shown in Fig. 9(c) whereas cross-sectional line plots together with the effective field components are shown in Figs. 9(d) and 9(e). For this mode, the out-of-plane amplitude is substantial, reaching $0.2M_s$ and the dynamical out-of-plane effective field component is large in magnitude [Figs. 9(d) and 9(e)]. Further, since the breathing of the y -domains is in-phase, the oscillation profile in Fig. 9(e) is antisymmetric, i.e., there is no difference in width or amplitude between the left and right part of the oscillation. The β mode has as we saw earlier four oscillating m_z components and to sample images at the oscillation turning points we have tagged five regions (see inset). We notice here a slightly tilted shape of the oscillations indicating a difference in increase and decrease time. There is therefore a slight time dependence in the phase relation between the lower part (regions C and D in the inset) and the top part (regions A and B in the inset) with a period of a half cycle. Figure 9(g) shows that the y -domains have an out-of-phase wobbling/tilting behavior, whereby they tilt in the opposite direction at any point in time. Further, Fig. 9(h) indicates that each y -domain actually has a substantial average tilting out-of-plane along y (with opposite relative tilting slopes for the $+y$ and $-y$ -domain). This is seen more clearly

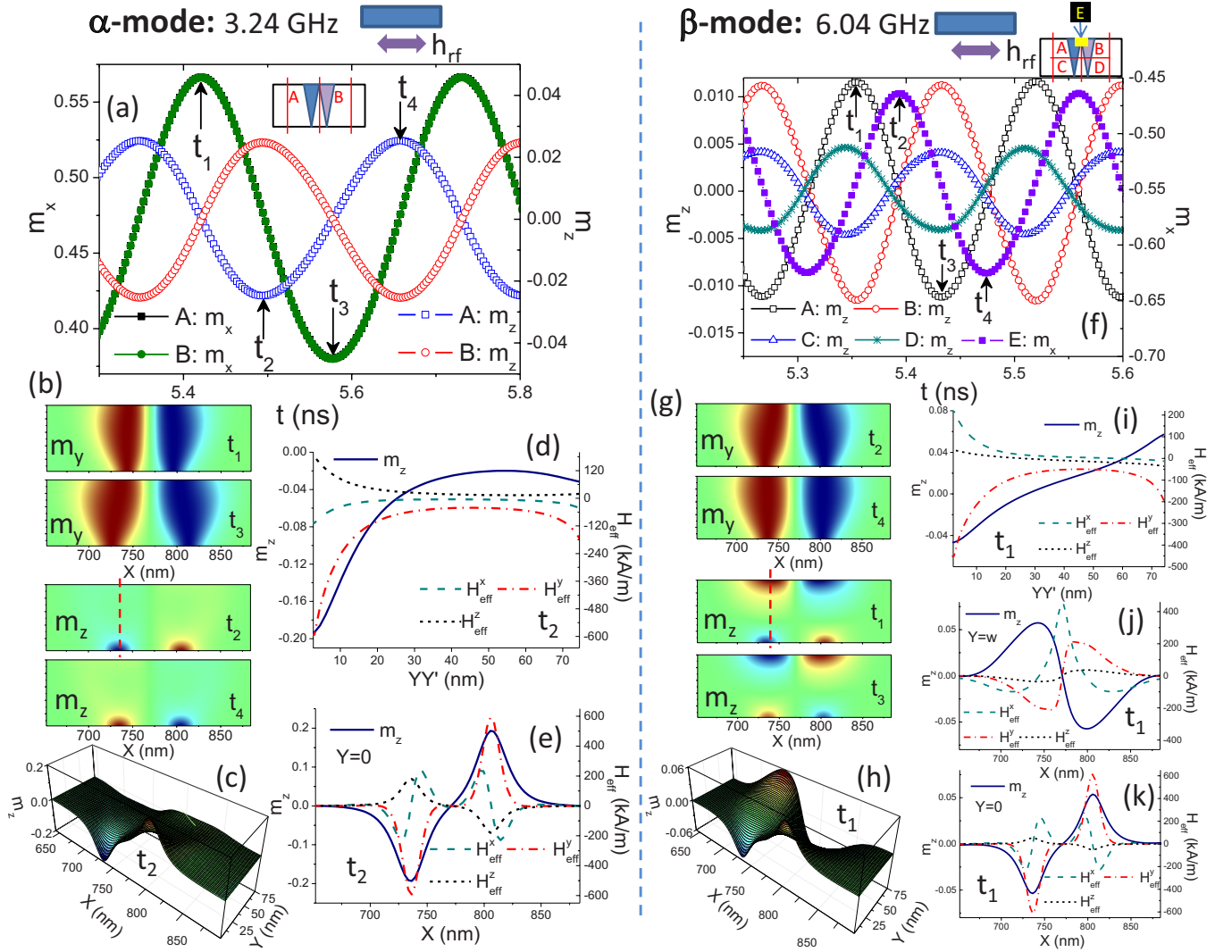


FIG. 9. (Color online) Time domains snapshots of the α and β modes during field driving at their resonance frequencies by a 5 Oe field along x . Left half: (a) the volume-averaged m_x and m_z components versus t of regions A and B within a time window during steady state. Regions A and B are schematically shown in the inset. Points t_1 - t_4 are times where the magnetization distribution has been extracted and plotted. (b) Time snapshots of the spatial distribution of m_y and m_z in the DW region taken at time points defined in (a). (c) A 3D plot of m_z at t_2 . (d) Line plots of the dynamic m_z and $H_{\text{eff}}^{x,y,z}$ at t_2 along a cross-section defined in (b) by the vertical red dashed line. (e): Line plots of m_z and $H_{\text{eff}}^{x,y,z}$ on $Y=0$ taken at t_2 . Right half: (f) the volume-averaged m_z and m_x components versus t of regions A-E within a time window during steady state driven oscillation. The tagged regions are shown in a schematic on the top right of the graph. Spatial distributions of m_y and m_z are taken at times t_1 - t_4 . (g) Snapshots of m_y and m_z taken in the DW area at times t_1 - t_4 . (h) 3D plot of m_z at t_1 . (i) Line plot of the dynamical m_z and $H_{\text{eff}}^{x,y,z}$ on a cross section as defined by the red dashed vertical line in (g). (j) Line plot at t_1 of m_z and $H_{\text{eff}}^{x,y,z}$ on $Y=w$. (k) As in (j) but on $Y=0$.

in Fig. 9(i), where a cross section YY' of the dynamical m_z component along with the dynamical effective fields are shown. Figs. 9(j) and 9(k) display cross sections of m_z and the effective field components giving an idea of the spatial extension along x of the mode profile. Shown clearly here is the relatively smeared H_{eff}^y profile on $Y=w$ as compared to $Y=0$. Thus the oscillations on $Y=w$ have a larger lateral extension along x . Again, as in the driven α case, the mode profiles indicates that any y -domain breathing occurs in-phase as the width and shape of the line profiles are (by eye) antisymmetrical. The methods and procedure to visualize driven dynamics when $\mathbf{h}_{\text{rf}} \parallel \mathbf{y}$ is exactly the same as for the previous driving cases. The result of driving the θ and ι

modes are shown in Fig. 10. For the θ case, the y -domains are also wobbling [Fig. 10(b)] as for β but this motion is now in-phase (i.e., tilting in the same directions for any point in time). Looking at Fig. 10(c) the profile exhibits an out-of-plane angle throughout the y direction, i.e., there are no flat parts of the profile running through a y -domain. The oscillating m_z components on $Y=0$ are in-phase but out-of-phase with the one on $Y=w$ [compare Figs. 10(d) and 10(e)]. The line profiles shown in Fig. 10(d) show perfect symmetry between region B and C indicating that if there is a subtle breathing of the y -domains it is in-phase. The driven ι mode differs substantially from the others. In this case there are no pronounced maxima on $Y=0$ and instead, most of region III

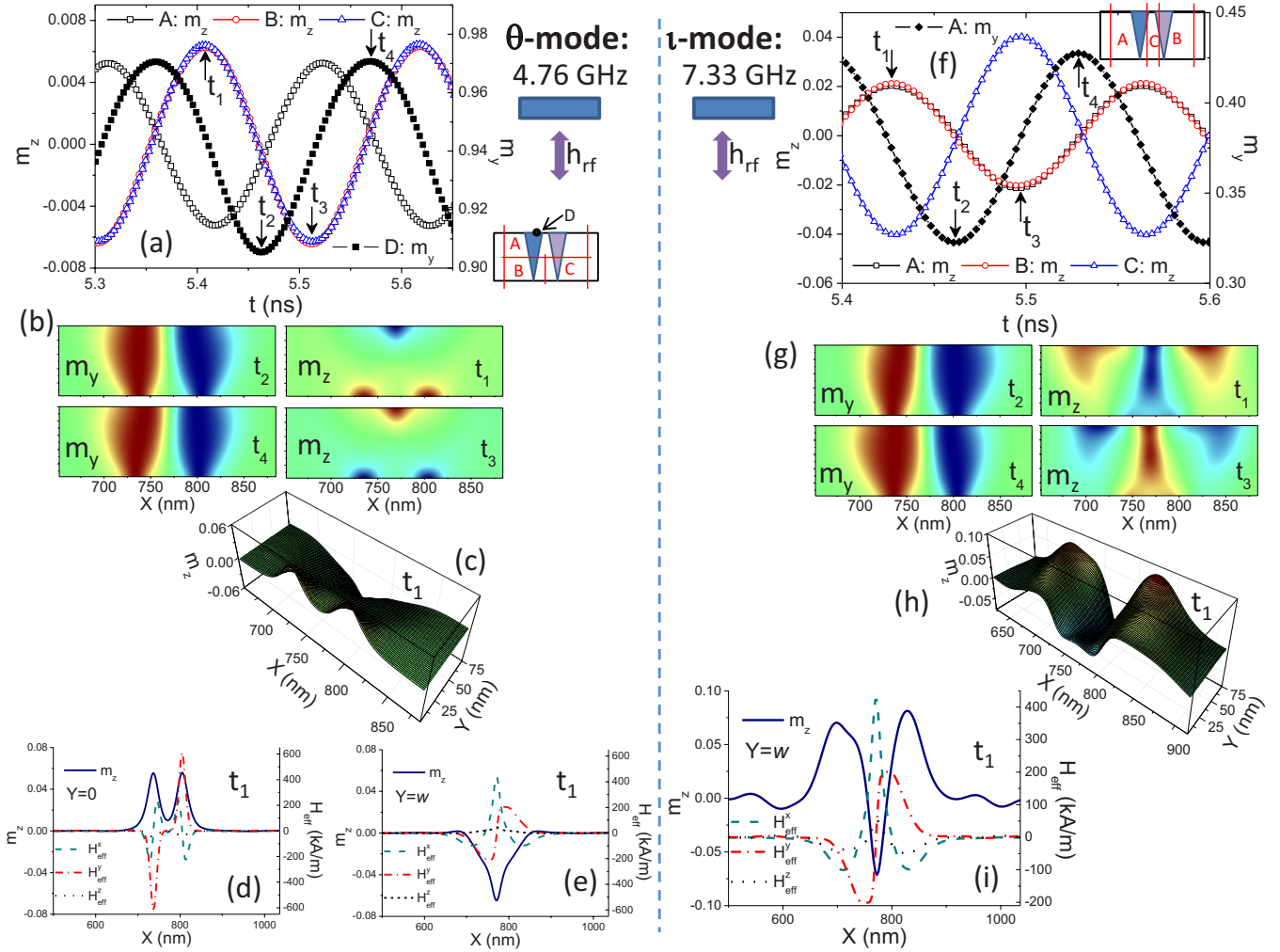


FIG. 10. (Color online) Time domains snapshots of the θ and ι modes during field driving at their resonance frequencies by a 5 Oe field along \hat{y} . Left half: (a) m_z and m_x components versus t of regions A–C (volume averaged) and the point D, within a time window during steady-state oscillation. Regions A–C and point D are schematically shown in the inset. Points t_1 – t_3 are times where the magnetization distribution have been extracted and plotted. (b) Time snapshots of the spatial distribution of m_y and m_z in the DW region taken at time points defined in (a). (c) A 3D plot of m_z at $t=t_1$. (d) Line plot at $t=t_1$ of m_z and $H_{\text{eff}}^{x,y,z}$ on $Y=0$. (e) As in (d) but on $Y=w$. Right half: (f) the volume-averaged m_z and m_x components versus t of regions A–C (as shown in the inset), within a time window during steady-state-driven oscillation. t_1 – t_4 define time points where magnetization distributions have been extracted. (g) Snapshots of m_y and m_z in the DW area at points in time according to (f). (h) 3D plot of m_z at $t=t_1$. (i) Line plot at $t=t_1$ of m_z and $H_{\text{eff}}^{x,y,z}$ on $Y=w$.

and the (I-II) and (IV-V) DWs are activated. The y -domains display a strong breathing behavior which is out-of-phase with respect to each other. This reflects in the mode profile seen in Fig. 8(i), whereby at this particular instance in time (t_1 in the figure), the $+y$ -domain is expanded and the $-y$ -domain is contracted, thus causing the relative asymmetry in shape at any point in time of the (I-II) and (IV-V) profile.

In conclusion, we have studied spin-wave eigenmodes of a 360° DW in a permalloy stripe for two different excitation directions and subsequently characterized its behavior when resonantly driving it for a set of different frequencies. With respect to the observed eigenmodes we have found that (i) low-frequency modes below the traveling SW band gap localize at the lateral edges of the y -domains and in the constituent DWs, (ii) there is strong dynamic dipolar coupling between the oscillating components, (iii) above the traveling

SW band gap, the 360° DW and EDs radiate SWs which causes mode splitting. The same holds for SWs excited in other parts of the stripe (i.e., case II), (iv) geometrical-type quantization effects imposed by the constituent DWs appear to be relatively weak in this case. (v) Within a broad frequency interval, there are strong indications of a high degree of mode hybridization between domain and DW modes and (vi) resonant driving at the four lowest modes reveal overall in-plane behaviors of the 360° DW such as translational, wobbling and breathing. Knowledge such as this may be of great use when designing devices using 360° DW in applications such as SW radiators, SW phase shifters, and memory devices.

ACKNOWLEDGMENTS

The authors acknowledge the CamGrid computing facilities for parts of the calculations.

*per24@cam.ac.uk

- ¹R. McMichael and M. J. Donahue, *IEEE Trans. Magn.* **33**, 4167 (1997).
- ²R. Hertel, W. Wulfhekel, and J. Kirschner, *Phys. Rev. Lett.* **93**, 257202 (2004).
- ³M. D. Mascaró, C. Nam, and C. A. Ross, *Appl. Phys. Lett.* **96**, 162501 (2010).
- ⁴A. Kunz, *Appl. Phys. Lett.* **94**, 132502 (2009).
- ⁵S. J. Hermsdoerfer, H. Schultheiss, C. Rausch, S. Schafer, B. Leven, S.-K. Kim, and B. Hillebrands, *Appl. Phys. Lett.* **94**, 223510 (2009).
- ⁶C. B. Muratov and V. V. Osipov, *J. Appl. Phys.* **104**, 053908 (2008).
- ⁷M. A. Shamsutdinov and V. N. Nazarov, *Phys. Met. Metallogr.* **107**, 569 (2009).
- ⁸P. E. Roy and P. Svedlindh, Contribution to the NIST μ MAG standard problem no. 4 at <http://www.ctcms.nist.gov/rdm/mumag.org.html>
- ⁹M. J. Donahue and D. G. Porter, National Institute of Standards and Technology Interagency Report No. NISTIR 6376, September 1999, <http://math.nist.gov/oommf/>.
- ¹⁰See supplementary material at <http://link.aps.org/supplemental/10.1103/PhysRevB.82.134411> for movies of the m_y and m_z -components during field-driven oscillation and results of a benchmark test problem comparison between our code and the OOMMF package.
- ¹¹M. J. Donahue and D. G. Porter, *Physica B* **343**, 177 (2004).
- ¹²J. Miltat, G. Albuquerque, and A. Thiaville, in *Spin Dynamics in Confined Magnetic Structures I*, Topics in Applied Physics Vol. 83, edited by B. Hillebrands and K. Ounadjela (Springer-Verlag, Berlin, 2002), Chap. 1.
- ¹³A. J. Newell, W. Williams, and D. J. Dunlop, *J. Geophys. Res.* **98**, 9551 (1993).
- ¹⁴L. Landau and E. Lifshitz, *Phys. Z. Sowjetunion* **8**, 153 (1935).
- ¹⁵A. Bagnères and S. Durbiano, *Comput. Phys. Commun.* **130**, 54 (2000).
- ¹⁶W. H. Press, B. P. Flannery, S. A. Teukolsky, and W. T. Vetterling, *Numerical Recipes: The Art of Scientific Computing* (Cambridge University Press, Cambridge, England, 1988).
- ¹⁷J. R. Cash and A. H. Karp, *ACM Trans. Math. Softw.* **16**, 201 (1990).
- ¹⁸A. Romeo, G. Finocchio, M. Carpentieri, L. Torres, G. Gonsolo, and B. Azzerboni, *Physica B* **403**, 464 (2008).
- ¹⁹R. D. McMichael and M. D. Stiles, *J. Appl. Phys.* **97**, 10J901 (2005).
- ²⁰S. McVitie and G. S. White, *J. Phys. D* **37**, 280 (2004).
- ²¹S. McVitie and M. Cushley, *Ultramicroscopy* **106**, 423 (2006).
- ²²J. Jorzick, S. O. Demokritov, B. Hillebrands, M. Bailleul, C. Fermon, K. Y. Guslienko, A. N. Slavin, D. V. Berkov, and N. L. Gorn, *Phys. Rev. Lett.* **88**, 047204 (2002).
- ²³C. Bayer, S. O. Demokritov, B. Hillebrands, and A. N. Slavin, *Appl. Phys. Lett.* **82**, 607 (2003).
- ²⁴M. Bailleul, R. Hollinger, and C. Fermon, *Phys. Rev. B* **73**, 104424 (2006).
- ²⁵M. Bailleul, R. Hollinger, K. Perzlmaier, and C. Fermon, *Phys. Rev. B* **76**, 224401 (2007).
- ²⁶M. Yan, G. Leaf, H. Kaper, R. Camley, and M. Grimsditch, *Phys. Rev. B* **73**, 014425 (2006).
- ²⁷G. Gubbiotti, M. Madami, S. Tacchi, G. Carlotti, M. Pasquale, N. Singh, S. Goolaup, and A. O. Adeyeye, *J. Phys.: Condens. Matter* **19**, 406229 (2007).
- ²⁸P. S. Keatley, V. V. Kruglyak, A. Neudert, E. A. Galaktionov, R. J. Hicken, J. R. Childress, and J. A. Katine, *Phys. Rev. B* **78**, 214412 (2008).
- ²⁹F. Montoncello, L. Giovannini, F. Nizzoli, H. Tanigawa, T. Ono, G. Gubbiotti, M. Madami, S. Tacchi, and G. Carlotti, *Phys. Rev. B* **78**, 104421 (2008).
- ³⁰F. Montoncello, L. Giovanni, and F. Nizzoli, *J. Appl. Phys.* **103**, 083910 (2008).
- ³¹K. Y. Guslienko, R. W. Chantrell, and A. N. Slavin, *Phys. Rev. B* **68**, 024422 (2003).
- ³²Y. Roussigne, S. M. Cherif, and P. Moch, *J. Magn. Magn. Mater.* **263**, 289 (2003).
- ³³M. Grimsditch, L. Giovannini, F. Montoncello, F. Nizzoli, G. K. Leaf, and H. G. Kaper, *Phys. Rev. B* **70**, 054409 (2004).
- ³⁴S.-S. Ha, J. Yoon, S. Lee, C.-Y. You, M.-H. Jung, and Y. K. Kim, *J. Appl. Phys.* **105**, 07D544 (2009).
- ³⁵J. P. Park, P. Eames, D. M. Engebretson, J. Berezovsky, and P. A. Crowell, *Phys. Rev. B* **67**, 020403 (2003).
- ³⁶K. Perzlmaier, M. Buess, C. H. Back, V. E. Demidov, B. Hillebrands, and S. O. Demokritov, *Phys. Rev. Lett.* **94**, 057202 (2005).
- ³⁷S. Macke and D. Goll, *J. Phys.: Conf. Ser.* **200**, 042015 (2010).
- ³⁸M. Bolte, G. Meier, and C. Bayer, *Phys. Rev. B* **73**, 052406 (2006).
- ³⁹V. V. Kruglyak, P. S. Keatly, R. J. Hicken, J. R. Childress, and J. A. Katine, *J. Appl. Phys.* **99**, 08F306 (2006).